Electrical transport, magnetic, and thermodynamic properties of La-, Pr-, and Nd-doped BaSnO₃₋δ single crystals

Eric McCalla,[1,2] Daniel Phelan,[3,*] Matthew J. Krogstad,[3,4] Bogdan Dabrowski,[4] and Chris Leighton[1,*]

[1]*Department of Chemical Engineering and Materials Science, University of Minnesota, Minneapolis, Minnesota 55455, USA*
[2]*Department of Chemistry, McGill University, Montréal, Québec, Canada H3A 0B8*
[3]*Materials Science Division, Argonne National Laboratory, Argonne, Illinois 60439, USA*
[4]*Department of Physics, Northern Illinois University, DeKalb, Illinois 60115, USA*

Due to outstanding room temperature electron mobility, the wide-gap perovskite semiconductor $BaSnO_3$ is of high current interest. Although n doping with Sb and O vacancies has been reported, most work has focused solely on La doping. Here we report bulk single crystals of $Ba_{1-x}R_xSnO_{3-\delta}$ with $R =$ La, Pr, and Nd, as well as unintentionally doped $BaSnO_{3-\delta}$, thus exploring new rare earth (magnetic) dopants in addition to O vacancy doping. Consistent with recent results on epitaxial films, O vacancies are shown capable of generating mid-10^{19} cm^{-3} Hall electron densities, with single crystal mobilities $\sim$100–150 cm^2 V^{-1} s^{-1}. Despite apparent solubility limits below $\sim$0.5 at. %, Pr and Nd are also shown to be effective n dopants, yielding Hall electron densities $>1 \times 10^{20}$ cm^{-3}, and ambient and low temperature mobilities up to 175 and 430 cm^2 V^{-1} s^{-1}, respectively. In contrast to the La-doped case, clear paramagnetism occurs with Pr and Nd doping, allowing for direct estimates of dopant concentrations for quantitative comparison with Hall densities. We show that dopant and Hall densities can be approximately reconciled, but only after accounting for O vacancy doping. Specific heat measurements were also performed, confirming the $BaSnO_3$ Debye temperature, and revealing electronic contributions roughly consistent with reported effective masses. Interestingly, and likely related to crystalline electric field effects, Pr-doped $BaSnO_3$ exhibits large deviations from simple Curie-Weiss susceptibility, and a pronounced Schottky anomaly, which we analyze in detail. These results provide significant insight into doping in $BaSnO_3$, establishing new rare earth magnetic dopants, clarifying the role of O vacancies, and determining dopant concentrations and solubility limits.

I. INTRODUCTION

The perovskite oxides are well known as a class of materials that combine extraordinary chemical flexibility with staggering diversity in physical properties [1]. Perovskites are thus a potential platform for the development of an all-oxide brand of electronics based on epitaxial heterostructures [2–4]. High mobility perovskite oxide semiconductors would be an attractive component in such structures, being of additional interest for low temperature quantum transport phenomena, such as the fractional quantum Hall effect [5,6]. Wide band gap versions of such high mobility perovskites would also be of interest in terms of transparent conductive oxides, power electronics, etc., particularly if high mobility could be maintained at room temperature. While stannate perovskites such as $CdSnO_3$ [7] and $ZnSnO_3$ [8] generated some interest in the past in this regard, recently *alkaline earth stannates*, in particular $BaSnO_3$, have attracted more attention [9–12]. $BaSnO_3$ single crystals have been reported to not only support room temperature electron mobility (μ) up to 320 cm^2 V^{-1} s^{-1}, but to maintain this high μ to unusually high free electron densities (n), resulting in outstanding conductivity [9–11]. At room temperature these μ values exceed those in $SrTiO_3$ [13],

for example, by a factor of $\sim$50, at a band gap in excess of 3 eV, generating much interest [9–11].

The high μ in these stannate perovskites is thought to derive in part from the small electron effective mass (m_e^*), which originates from significant dispersion of the Sn 5s states at the conduction band minimum [10,14–19]. Theoretical values from density functional theory vary substantially, from 0.028 to 0.47 m_0 (where m_0 is the free electron mass) [12,14,16–20], as do experimental values to some extent (from 0.14 to 0.61 m_0) [21–28], but a relatively low m_e^* for a perovskite oxide semiconductor is supported; recent experimental determinations cluster around $m_e^* \approx 0.2 m_0$ [25–27]. Scattering rates are, of course, the other key factor. In $BaSnO_3$ single crystals, recent theoretical work has quantitatively understood the room temperature μ in terms of unusually low phonon scattering rates, combined with ionized impurity scattering [15]. In epitaxial films, μ values lag those in single crystals, although rapid progress is being made [29–39]. This lag is thought to derive from additional dislocation scattering in films, due to the large lattice mismatches with commercially available substrates [30–39]. Many scattering sources in $BaSnO_3$ have thus been investigated, including phonons [11,12,14,15,39,40], ionized impurities [10,12,28,39], neutral impurities [12,28], and dislocations [30–39]; various point defects have also been considered [19,41]. Importantly, recent work has succeeded in a doping-dependent determination of

*Corresponding authors: dphelan@anl.gov; leighton@umn.edu

the mobility-limiting scattering mechanisms in epitaxial films [39].

While epitaxial films are required for incorporation in oxide heterostructures, for potential μ increases by modulation/remote doping, and for applications as a transparent conductor, for example, single crystals remain important. They can be used as a model platform to study intrinsic physical properties, to explore new potential dopants, and to elucidate mobility-limiting scattering mechanisms. With regard to dopants, in single crystals, n-type doping has thus far been achieved through La^{3+} substitution for Ba^{2+} [9–11,42], Sb^{5+} substitution for Sn^{4+} [28], and by introduction of oxygen vacancies (V_O) [42,43]. Surveying the literature, the highest room temperature μ reported ($320\,cm^2\,V^{-1}\,s^{-1}$) was found in a La-doped crystal (i.e., $Ba_{1-x}La_xSnO_3$) from Kim *et al.* that was grown from Cu_2O flux [9]. Significant crystal-to-crystal variance in μ was reported by many of the same authors, however, with μ showing little to no dependence on n [10]. Unintentionally doped (UD) $BaSnO_{3-\delta}$ crystals grown by the Cu_2O flux method have also been shown to be conductive [43], and ascribed to V_O doping; insulating crystals were obtained by addition of $KClO_4$ into a $CuO + Cu_2O$ flux [33]. V_O doping has been reported in epitaxial films also [34,35], and was recently studied systematically as a function of vacuum reduction temperature [35]. Complementary to the above, Sb doping on the Sn site, i.e., in $BaSn_{1-x}Sb_xO_3$, has been studied via crystal growth, again using Cu_2O flux. Room temperature μ as high as $79\,cm^2\,V^{-1}\,s^{-1}$ was reported at $n = 1 \times 10^{20}\,cm^{-3}$ [28]. Alternative crystal growth methods have also been demonstrated. For example, Luo *et al.* employed an alternative (PbO-based) flux to grow $Ba_{1-x}La_xSnO_3$ and reported $\mu = 103\,cm^2\,V^{-1}\,s^{-1}$ at $n = 8 \times 10^{19}\,cm^{-3}$ [11]. Additionally, Galazka *et al.* recently reported growth of undoped and La-doped $BaSnO_3$ crystals directly from the melt [42]. They obtained both insulating and conductive crystals without La substitution and reported $\mu = 220\,cm^2\,V^{-1}\,s^{-1}$ at $n = 3.3 \times 10^{19}\,cm^{-3}$ for La-doped crystals.

While progress has thus been made with La, Sb, and V_O doping, there clearly exists room for exploration of additional potential n dopants in $BaSnO_3$, which is one of the main goals of this work. Rare earths are particularly appealing, as the introduction of magnetism could provide new opportunities. Although rare-earth-doped bulk single crystals have not been reported to our knowledge, Gd-doped $BaSnO_3$ epitaxial films have. Alaan *et al.* realized $\mu \approx 30\,cm^2\,V^{-1}\,s^{-1}$ at room temperature in $Ba_{0.96}Gd_{0.04}SnO_3$ films, the field dependence of the magnetization (M) being well described by a Brillouin function with $g = 2$ and $J = 7/2$ for Gd [44]. While 4% substitution is perhaps unlikely in bulk crystals, this result is encouraging for synthesis of rare-earth-doped $BaSnO_3$ crystals, particularly with larger ionic size dopants, closer to La^{3+}. The ideal paramagnetism observed in $Ba_{0.96}Gd_{0.04}SnO_3$ [44] also points to the possibility of using magnetometry to estimate the actual donor concentration, N_{donor}. This is nontrivial for nominally nonmagnetic La, Sb, and V_O dopants, where there is no straightforward means to determine the actual N_{donor} value. Doing this could provide compensation ratios by comparison with measured n values, and an assessment of whether other dopants, such as V_O, coexist with deliberate substitutional doping.

Motivated by the above, particularly the need to explore additional dopants in $BaSnO_3$ and establish methods for determination of N_{donor}, we have investigated Pr and Nd doping in $BaSnO_3$ bulk single crystals. While dopant incorporation is limited to $\sim0.5\,at.\%$, both ions are shown to be effective n dopants, yielding n and μ values comparable to La doping. Nd doping further results in near-ideal noninteracting paramagnetic response to both magnetic field (H) and temperature (T), enabling direct estimation of N_{donor}. The N_{donor} values can be approximately reconciled with the measured n, assuming negligible compensation at these doping levels, but only *provided* that V_O doping is also taken into account. The latter is also probed here, in unintentionally doped (UD) crystals. Specific heat measurements are additionally presented, providing a $BaSnO_3$ Debye temperature, and an electronic contribution roughly consistent with reported m_e^* values. Pr doping, on the other hand, leads to marked deviations from Curie-Weiss behavior, and a pronounced Schottky anomaly in specific heat, which we associate with crystalline electric field effects.

II. METHODS

Single crystals of $BaSnO_{3-\delta}$ and $Ba_{1-x}R_xSnO_{3-\delta}$ with $R =$ La, Pr, and Nd were grown via flux growth. Polycrystalline starting materials were first prepared using standard solid-state reaction, with 1%–2% R content. All such R-doped starting materials contained secondary pyrochlore $R_2Sn_2O_7$ phases, suggesting a low solubility limit, consistent with a reported $La_2Sn_2O_7$ impurity in $Ba_{1-x}La_xSnO_3$ polycrystalline samples [11]. Although the pyrochlore phase fraction is difficult to quantify at these levels via lab x-ray diffraction, it does appear to increase with decreasing R ionic size. Flux growth was performed from these 1%–2%-doped (nominal charge value) polycrystalline materials mixed in a Cu_2O flux, following procedures similar to those previously described [43]. Specifically, crystals were grown by slow cooling the flux and charge ($\sim40 : 1$ ratio) in Pt crucibles that had been heated in air beyond the flux melting point. After growth, faceted single crystals were clearly visible after removal from the flux with dilute nitric acid. The maximum size of the crystals was $\sim70\,mg$. The larger UD crystals were translucent but possessed a darkish hue, while thin ($\sim100s$ of μm) UD crystals were transparent; typically sized R-doped crystals were noticeably darker. Structural quality was verified by single crystal x-ray diffraction on beamline A2 of the Cornell High Energy Synchrotron Source (CHESS), using an energy of 56.7 keV. For UD crystals, attempts were made to both thermally reduce and oxidize crystals. Annealing treatments were performed under various conditions, from vacuum (down to 10^{-8} Torr), to flowing O_2, to high pressure O_2 (240 atm), at temperatures between 550 and $1100\,°C$. Specific conditions in each case are given in Table I.

Electronic transport measurements were performed in a van der Pauw geometry, down to 1.5 K and in fields up to 9 T. Crystals were first polished to $\sim0.5\,mm$ thick plates, before sputtering Au contacts with a thin Al adhesion layer. Such contacts were Ohmic at the current densities used, at all temperatures. Magnetometry was performed using a Quantum Design Magnetic Property Measurement System (MPMS), down to 5 K and in fields up to 9 T; higher temperature measurements (to

TABLE I. Electronic transport parameters of various $Ba_{1-x}R_xSnO_{3-\delta}$ single crystals studied in this work. T_{ann} is the temperature at which post-growth annealing was performed (no entry indicates no annealing was performed), n is the Hall electron density, ρ is resistivity, and μ is the electron mobility. Note that UD = unintentionally doped, and that crystals UD1 and UD2 are from the same growth batch; for UD2 the three measurements shown are in chronological order.

Sample	T_{ann} (°C)	Anneal atmosphere	n(300 K) (cm^{-3})	ρ(5 K) (mΩ cm)	ρ(300 K) (mΩ cm)	μ(5 K) (cm^2 V^{-1} s^{-1})	μ(300 K) (cm^2 V^{-1} s^{-1})
UD1	–	–	3.02×10^{19}	2.01	2.47	102	83
UD1	1100	10^{-6} Torr	3.07×10^{19}	1.98	2.38	102	81
UD2	–	–	3.56×10^{19}	1.63	2.02	106	86
UD2	1000	1 atm O_2[a]	2.15×10^{19}	2.94	3.61	100	80
UD2	1000	2×10^{-8} Torr	2.24×10^{19}	2.73	3.16	100	88
UD3	550	240 atm O_2	3.27×10^{19}	1.30	1.80	145	106
La-doped	–	–	3.36×10^{20}	0.150	0.226	120	78
Pr-doped	–	–	1.12×10^{20}	0.155	0.328	357	170
Nd-doped	–	–	1.11×10^{20}	0.118	0.322	434	174

[a]Cooled slowly (0.1 K/min) after annealing; all other annealed samples were cooled at an average rate of 5 K/min or faster.

900 K) were made using the oven option of a Quantum Design MPMS-3 system. Specific heat (C_p) measurements were performed in Quantum Design Physical Property Measurement Systems (PPMSs), either to 1.8 or 0.4 K, using relaxation calorimetry. The heat pulse used was 2% of the measurement temperature. In all cases, Apiezon N grease was used to affix the samples, addenda were carefully subtracted, and sample/addenda heat capacity ratios were maintained at acceptable levels [45]. Sample/calorimeter thermal couplings were kept above the 90% Quantum Design recommendation, except for the Pr-doped sample above 4 K, which slipped below 90%.

III. RESULTS AND DISCUSSION

Figure 1(a) shows the synchrotron x-ray diffraction pattern collected from a representative Nd-doped crystal, the high incident energy ensuring illumination of the bulk, as opposed to just the surface. The pattern confirms single crystallinity and can be indexed to the cubic $Pm\bar{3}m$ space group, consistent with perovskite BaSnO$_3$. Such analysis yields a lattice parameter of $a = 4.114 \pm 0.002$ Å, with an upper bound on the mosaic spread of 0.2°. Note that the latter is limited by the angular step size in the measurement, however, and that the true value may well be considerably smaller. Within uncertainty, the lattice parameter is identical to the accepted value for BaSnO$_3$ (4.116 Å) [10,11]. This indicates that the extent of Nd^{3+} substitution for Ba^{2+} is likely small, as lattice expansion with doping with La^{3+}, for instance, has been documented [10,11]. While the close agreement with the accepted lattice parameter is a positive indication, defects due to cation nonstoichiometry cannot be ruled out at semiconductor doping levels.

Table I and Figs. 1(b)–1(d) summarize the results of transport measurements on these crystals. Two as-grown UD crystals are reported in Table I (denoted UD1 and UD2), both of which were found to be conductive. At room temperature, one had $n = 3.02 \times 10^{19}$ cm^{-3} and $\mu = 83$ cm^2 V^{-1} s^{-1}, the other $n = 3.56 \times 10^{19}$ cm^{-3} and $\mu = 86$ cm^2 V^{-1} s^{-1}. As shown in Figs. 1(b) and 1(c) these crystals exhibit degenerate behavior (n essentially independent of T), with μ that increases to 102–106 cm^2 V^{-1} s^{-1} on cooling. Corresponding resistivity (ρ) values drop on cooling from 2.47 and 2.02 mΩ cm to

2.01 and 1.63 mΩ cm, respectively, giving residual resistivity ratios (RRRs) of ~1.2–1.3. Consistent with prior work on bulk single crystals [43] and epitaxial thin films [34,35], we ascribe this n-type conduction in UD crystals to V$_O$ doping. Explicitly, we interpret these results in terms of the chemical formula BaSnO$_{3-\delta}$, with each V$_O$ donating two electrons to the conduction band in the simplest picture. Using a lattice parameter of 4.116 Å, the n values in UD1 and UD2 then correspond to δ values of 0.0010 and 0.0013; such small values are difficult to determine by other means.

As can be seen from Table I, the n values in as-grown UD crystals are consistently in the mid-10^{19} cm^{-3} range, similar to that seen in epitaxial films reduced at ~900 °C [34,35]. To probe the possibility of manipulating (post-growth) the density of V$_O$, and thus the n-doping level, these UD crystals were subjected to various thermal treatments, as summarized in Table I. Sample UD1, for instance, was annealed in high vacuum (10^{-6} Torr) at 1100 °C in an attempt to reduce it. This resulted in negligible change in transport, however, with n only shifting from 3.02×10^{19} to 3.07×10^{19} cm^{-3}. Similarly, sample UD2 was annealed in flowing O$_2$ at 1000 °C and then slowly cooled (0.1 K/min) in an attempt to oxidize it, but n only decreased from 3.56×10^{19} to 2.15×10^{19} cm^{-3}. Very high vacuum (10^{-8} Torr) annealing at 1000 °C also induced little change in n, and even high pressure (240 atm) O$_2$ annealing at 550 °C resulted in little change in transport properties. In contrast to bulk single crystal SrTiO$_3$ [13], post-growth annealing is thus ineffective in manipulating V$_O$ doping in BaSnO$_{3-\delta}$, the V$_O$ density apparently being locked in during growth. The δ values in BaSnO$_{3-\delta}$ are thus fixed by the growth conditions and cooling trajectory. These results likely indicate that while the enthalpy of formation of V$_O$ in BaSnO$_3$ is small enough to generate significant doping during growth, the diffusivity of V$_O$ is low at typical annealing temperatures. Thin epitaxial films can thus be easily V$_O$ doped by post-growth annealing (the diffusion length need not be large), whereas bulk single crystals cannot. Additional defects in thin films could also play a role in V$_O$ kinetics.

Table I and Figs. 1(b)–1(d) also show representative examples of La-, Pr-, and Nd-doped BaSnO$_3$ crystals, all of which show significantly higher n than nominally UD crystals.
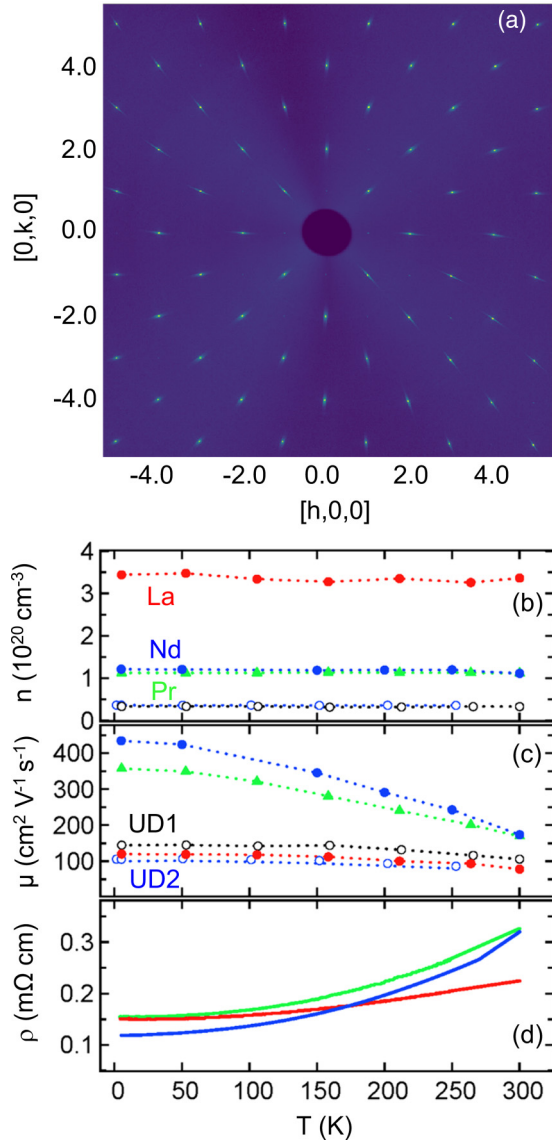
FIG. 1. (a) X-ray diffraction from a representative Nd-doped BaSnO$_3$ single crystal at 56.7 keV. Note that the streaks around each peak are a result of Compton scattering inside the Si detector, and do not reflect low crystalline quality. (b)–(d) Temperature (T) dependence of Hall electron density (n), Hall electron mobility (μ), and resistivity (ρ). Results are shown for La- (red filled symbols), Nd- (blue filled symbols), and Pr-doped crystals (green filled symbols), in addition to two unintentionally doped (UD) crystals, UD1 and UD2 (open symbols). UD1 and UD2 have resistivities somewhat larger than the substitutionally doped crystals, and are not shown in (c).

Roughly consistent with prior work [9–11,42], La doping induces $n = 3.36 \times 10^{20}$ cm^{-3}, which, assuming full dopant activation and negligible compensation, would correspond to 2.3% substitution, in very reasonable agreement with the La inclusion in the growth vessel. Room temperature μ values ~ 100 cm^2 V^{-1} s^{-1} were obtained in such La-doped samples. Also shown in Table I is that while Pr and Nd doping typically results in slightly lower n than for La, n-type doping with these R ions is clearly effective. n values $\sim 1 \times 10^{20}$ cm^{-3} were obtained with Nd and Pr, the room and low temperature

μ values reaching 175 and 434 cm^2 V^{-1} s^{-1}, respectively. Importantly, these mobilities are comparable to reported La-doped values [9–11,42], despite the slightly lower n. The latter likely indicates that the solubility of Nd and Pr is lower than La, resulting in N_{donor} less than the nominal 1%–2% loaded in the growth vessel; this is returned to below. As shown in Figs. 1(b)–1(d), $n(T)$ indicates degenerate doping in all three cases (La, Nd, Pr), $\mu(T)$ revealing the standard increase on cooling due to reduction of phonon scattering. $\rho(T)$ [Fig. 1(d)] thus shows metallic-like $d\rho/dT$, with the exception of very minor indications of weak localization at the lowest T. Low T resistivities down to 100–150 $\mu\Omega$ cm are obtained, with RRRs up to 2.7. Again, these values in Nd- and Pr-doped samples are comparable to the best obtained in La-doped crystals [9–11,42]. Given the substantial scatter in room temperature mobilities reported in doped BaSnO$_3$ crystals, potentially due to an uncontrolled density of nonstoichiometry-related defects, we do not interpret the factor of ~ 2 difference we find between La and Pr/Nd mobilities.

Figure 2 turns to the magnetic properties of these Nd- and Pr-doped BaSnO$_3$ crystals, which, as discussed in the Introduction, are of general interest, and can potentially offer a means to quantify N_{donor}. The main panel of Fig. 2(a) shows the magnetization M vs $1/T$ for a representative Nd-doped crystal, measured in $H = 10$ kOe. The behavior is linear and can be very well fit (solid line) to the Curie-Weiss Law for susceptibility (M/H), i.e.,

$$\chi = \frac{N m_{\mathrm{eff}}^2 / 3 k_B}{T - \theta}, \tag{1}$$

where N is the volume density of magnetic moments, m_{eff} is the effective moment ($g[J(J+1)]^{1/2} \mu_{\mathrm{B}}$), where g is the g factor, J is the total angular momentum quantum number, and μ_B is the Bohr magneton, k_B is Boltzmann's constant, and θ is the Curie-Weiss temperature. The fit yields $m_{\mathrm{eff}}^{\mathrm{meas}} = 0.185 \, \mu_{\mathrm{B}}$/formula unit (f.u.) and a Curie-Weiss temperature $\theta \approx 0$ K, indicating negligible interactions, i.e., reduction to the Curie Law. This is as expected for a low density of Nd dopants. Using the free-ion value for Nd^{3+} of $m_{\mathrm{eff}}^{\mathrm{theor}} = 3.62 \, \mu_{\mathrm{B}}$ [46], we can then estimate the density of Nd ions using $N_{\mathrm{Nd}} \approx (\frac{m_{\mathrm{eff}}^{\mathrm{meas}}}{m_{\mathrm{eff}}^{\mathrm{theor}}})^2$, which, from Fig. 2(a), yields 0.26 at. %, or 3.7×10^{19} cm^{-3}. A second estimate of N_{Nd} can be obtained from $M(H)$ at low T, as shown in Fig. 2(b) (at 5 K). The solid line there is a fit to a Brillouin function:

$$M = N g J \mu_B \left[\frac{2J+1}{2J} \coth\left(\frac{(2J+1) g \mu_B \mu_0 H}{2 k_B T} \right) \right.$$
$$\left. - \frac{1}{2J} \coth\left(\frac{g \mu_B \mu_0 H}{2 k_B T} \right) \right]. \tag{2}$$

The fit yields a magnetic moment (i.e., g and J values) that again corresponds to exactly 0.26 at. % Nd, in perfect agreement with the analysis of Fig. 2(a).

The situation in Pr-doped BaSnO$_3$ crystals is somewhat different. Specifically, in the 5–300 K range studied for the Nd case, the M vs $1/T$ behavior in Pr-doped samples is distinctly nonlinear, exhibiting a kink near ~ 50 K. As shown in the inset to Fig. 2(a), at higher T, however, between 300 and 900 K, Curie-Weiss behavior is recovered. The solid line fit
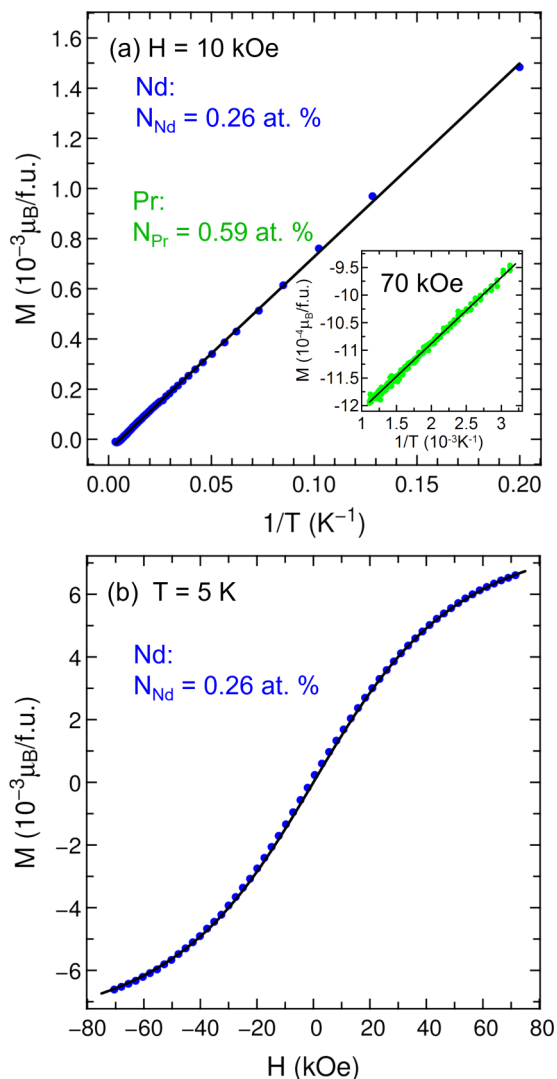
FIG. 2. (a) Magnetization (M) vs $1/T$ for a representative Nd-doped crystal (main panel, blue points) and a representative Pr-doped crystal (inset, green points). As described in the text, the main panel is from 5 to 300 K, the inset from 300 to 900 K. Solid lines are fits to the Curie-Weiss law, as discussed in the text. (b) M vs applied magnetic field (H) for the Nd-doped sample at 5 K, along with a Brillouin function fit. Shown are the rare earth concentrations (N_{Nd}, N_{Pr}) extracted from the respective fits.

shown there is to a sum of Curie-Weiss and T-independent diamagnetic contributions, yielding $m_{\text{eff}}^{\text{meas}} = 0.276\ \mu_{\text{B}}/\text{f.u.}$, corresponding (through a free-ion $m_{\text{eff}}^{\text{theor}}$ of $3.58\ \mu_{\text{B}}$ [46]) to $N_{\text{Pr}} = 0.59$ at. %, i.e., $8.4 \times 10^{19}\ \text{cm}^{-3}$, not dissimilar to N_{Nd}. Given the low density of Pr substitution, the low T non-Curie-Weiss behavior cannot arise from magnetic interactions, but is instead very likely due to the effects of the crystalline electric field on the single ion susceptibility. For the cubic point symmetry at the $\text{Pr}^{3+}(\text{Ba}^{3+})$ site the Hamiltonian representing the interaction with the crystalline electric field (H_{CEF}) can be written as a linear combination of four Stevens operator equivalents (O_n^m), with only two independent crystal field parameters (B_n^m) [47]:

$$H_{\text{CEF}} = B_4^0 O_4^0 + 5 B_4^0 O_4^4 + B_6^0 O_6^0 - 21 B_6^0 O_6^4. \quad (3)$$

What would otherwise be nine [$(2J+1)$ with $J=4$] degenerate states in the absence of H_{CEF} are thus split into two triplets, a doublet, and a singlet. The actual level scheme, however, depends on the specific values of B_4^0 and B_6^0, a fact that we discuss again below in relation to heat capacity data. Of most relevance to the $M(T)$ data, the net effect of the CEF splitting is that at low T the number of accessible states is reduced, meaning that a lower $m_{\text{eff}}^{\text{meas}}$ than the theoretical free-ion moment is expected. As is common in rare earth compounds, however, the high T susceptibility provides a viable means to determine an accurate effective moment, as the full moment recovers when thermal energy overcomes the crystal field splittings [48]. We believe this to be the origin of the linear behavior seen in the inset to Fig. 2(a) at high T, and thus that the extracted N_{Pr} is reliable. Note that the crystal field levels of Nd^{3+} ions in a cubic perovskite have not been well studied experimentally, although calculations for Nd-containing cobaltites yield a ground-state quartet [47]. This potentially explains why simple Curie-Weiss behavior is observed to significantly lower temperatures in the Nd-doped case.

Comparisons between N_{Pr}, N_{Nd}, and n are made below, to understand in further detail the doping in these systems. Prior to that, however, we note that low T specific heat offers another potential means to probe CEF splittings in the Pr-doped case, and thus to confirm the above conclusions. $C_{\text{P}}(T)$ at low T also provides access to lattice dynamics information, as well as the electronic contribution to C_P, and therefore m_e^*. Specific heat was thus measured down to 1.8 K on representative La-, Nd- and Pr-doped crystals, in addition to a UD crystal (UD4), as shown in the C_{P}/T vs T^2 plot in Fig. 3(a). The striking observation is of course the very different behavior of the Pr-doped crystal in comparison to all others. Specifically, the Pr-doped crystal shows much larger low T specific heat, apparently diverging as $T \to 0$ on this C_{P}/T vs T^2 plot, indicating substantial excess specific heat in comparison to UD, La-, and Nd-doped cases. The $C_{\text{P}}(T)$ of the UD, La, and Nd crystals in this T range can in fact be described [see fits in Fig. 3(a)] in a quite standard way, using

$$C_{\text{P}}(T) = \beta T^3 + \alpha T^5 + \gamma T + \frac{A}{T^2}. \quad (4)$$

βT^3 and αT^5 are first- and second-order Debye terms describing the lattice dynamic contributions to $C_{\text{P}}(T)$, where β is related to the Debye temperature θ_{D} through $\beta = 234 N_0 k_{\text{B}}/\theta_{\text{D}}^3$, and N_0 is the number of ions per mole. The γT term is the typical electronic contribution to $C_{\text{P}}(T)$, which, in the free-electron model, is related to the effective mass through $m_e^* = \gamma (3/\pi)^{2/3} \hbar^2 k_{\text{B}}^{-2} n^{-1/3}$. Finally, the A/T^2 term, which is required to describe the small upturn in the data at the lowest T for the La- and Nd-doped crystals, models the high T tail of a Schottky anomaly. Such Schottky anomalies are common in the very low T heat capacity of solids, arising due to any mechanism that produces a manifold of relatively low lying excited states, which generates peaks in $C_{\text{P}}(T)$ [49,50]. While this A/T^2 term is minor for the UD, La, and Nd cases, it is this term that becomes very large for the Pr-doped crystals, as discussed in detail below.

From the fits shown in Fig. 3(a) for the UD, La-doped, and Nd-doped cases, β, α, γ, and A were extracted, leading to
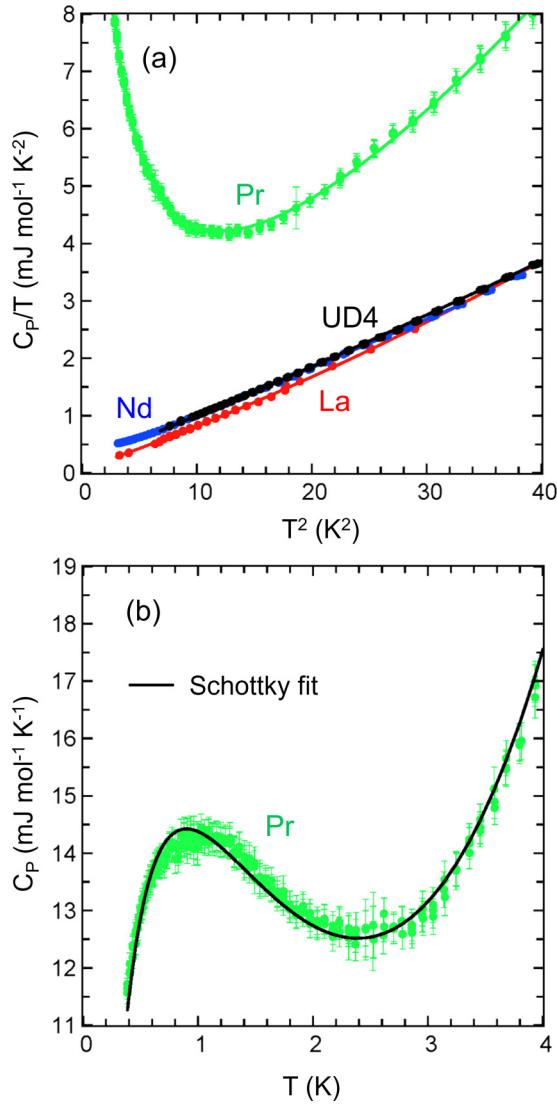
FIG. 3. (a) Temperature (T) dependence of the specific heat (C_P), plotted as C_P/T vs T^2 down to 1.8 K. Data are shown for a nominally undoped (UD) crystal (UD4), and a La-, Nd-, and Pr-doped crystal. Solid lines are fits to the model described in the text. (b) $C_P(T)$ for the Pr-doped crystal down to 0.4 K, along with a fit to the model described in the text. Fit parameters are shown in Table II, and are discussed in the text.

the θ_D, m_e^*, and A values reported in Table II. Considering the lattice terms first, we see from Table II that θ_D is approximately

TABLE II. Parameters extracted from fitting of low temperature heat capacity data (Fig. 3) for a Nd-doped crystal, a La-doped crystal, and an unintentionally doped (UD) crystal (UD4). θ_D is the Debye temperature, m_e^* is the electron effective mass, and A/T^2 is the heat capacity term used to describe the high temperature (T) tail of a Schottky anomaly.

Sample	θ_D (K)	m_e^*/m_0	A (J K mol^{-1})
Nd-doped	485 ± 20	0.35 ± 0.26	7.6×10^{-4}
La-doped	516 ± 20	0.19 ± 0.15	4.6×10^{-5}
UD4	497 ± 20	0.70 ± 0.60	0

constant, lying between 485 ± 20 and 516 ± 20 K. These values are in good general agreement with prior work, although there is significant scatter in existing estimates. Specifically, speed of sound data from polycrystalline ceramics indicate 522 K [51], DFT calculations yield 496 K [52], speed of sound data on single crystals yield 426 K in the continuum limit [11], and previous free-fitting of heat capacity of a single crystal yielded 377 K in the continuum limit [11]. We note here that recent inelastic neutron scattering measurements lend credence to the estimation from sound wave velocity measurements in polycrystalline materials [53]. The electronic contributions to C_P are small in comparison to the lattice contributions, due to the small Fermi surfaces here relative to typical metals, but nevertheless enable rough estimates of m_e^*. Using the free-electron approximation and the measured values of n this results in m_e^*/m_0 of 0.35 ± 0.26, 0.19 ± 0.15, and 0.70 ± 0.60 for the Nd, La, and UD cases, respectively. These electron effective masses average to $\sim 0.4\,m_0$, albeit with significant uncertainty; high accuracy, very low T measurements would be required to improve upon this. Extracted A values are also small, and in fact in the UD case the A/T^2 term was not even required to describe the data.

For the Pr-doped crystal alone, the A/T^2 term due to the high T tail of a Schottky anomaly becomes very large [see Fig. 3(a)], indicating that it arises from Pr ions. To investigate this in further detail, $C_P(T)$ measurements for the Pr-doped sample were extended down to 0.4 K, resulting in the data shown in Fig. 3(b). A Schottky anomaly is revealed in full detail, a clear peak in C_P occurring around 1 K. This peak can be adequately described [see the solid line fit in Fig. 3(b)] by the formula for a two-level system,

$$C_P^{\text{Schottky}}(T) = N_{\text{Pr}} R \left(\frac{\Delta E}{k_B T} \right)^2 \left(\frac{\nu_0}{\nu_1} \right) \frac{e^{\frac{\Delta E}{k_B T}}}{1 + \frac{\nu_0}{\nu_1} e^{\frac{\Delta E}{k_B T}}}, \quad (5)$$

where ν_0 and ν_1 are the degeneracies of the ground and excited states, ΔE is their energy splitting, and R is the molar gas constant [50]. Note here that (a) the A/T^2 term in Eq. (4) is simply the high T tail of a Schottky peak described by (5), and (b) that the amplitude of the Schottky anomaly described by (5) is controlled by N_{Pr}, i.e., the density of Schottky-active sites. Due to the significant number of parameters, and the dominance of the Schottky specific heat, two approaches were used to fit the data of Fig. 3(b), and the results compared. In the first, the A/T^2 term in Eq. (4) was replaced with the full Schottky term in (5) and the lattice and electronic terms constrained to generic values of $\theta_D = 500$ K and $m_e^* = 0.2\,m_0$. This results in $\Delta E = 1.96$ K $= 0.16$ meV, $N_{\text{Pr}} = 0.21$ at. %, and $\nu_0/\nu_1 = 3.15$. In the second method, all unknowns were treated as fitting parameters, yielding $\Delta E = 2.23$ K, $N_{\text{Pr}} = 0.43$ at. %, and $\nu_0/\nu_1 = 6.35$. Importantly, the extracted ΔE and N_{Pr} values from the two approaches differ relatively little, and, moreover, the N_{Pr} values of 0.21 to 0.43 at. %, are reasonably consistent with the 0.59 at. % from high T magnetometry.

In terms of *mechanisms* for the Schottky anomaly, the values of ΔE extracted are likely too large to arise from hyperfine splitting of the ^{141}Pr nuclear spin states [54,55]. Excitation from the ground CEF level to the first excited CEF level is instead more likely. For the crystal field parameters determined for a cubic Pr-containing cobaltite, the ground state

is a Γ_5 triplet [47], and we speculate that a local lowering of the site symmetry at the dopant site breaks what would be a triplet ground state by ~ 2 K, giving rise to the observed Schottky anomaly. It is possible, however, that the excitation occurs between different nondegenerate sublevels of a cubic crystal field in $BaSnO_3$, which we note has a significantly larger lattice constant than the cobaltite in Ref. [47], and hence possibly a different energy level scheme. In the absence of spectroscopic data, we leave open both of these possibilities.

The above magnetometry and heat capacity results provide solid estimates for N_{donor} in our Pr- and Nd-doped samples, which are difficult to obtain by other means. With these estimates of N_{Nd} and N_{Pr} in hand, we now return to the issues of R ion solubility limits, and comparisons with the Hall electron density n. We first note that the measured dopant concentrations in these single crystals (0.26 at. % for Nd, and an average of 0.41 at. % for Pr), unlike for La doping, are distinctly lower than the 1–2 at. % in the polycrystalline precursors used in the flux growth. One simple interpretation here is that the measured N_{donor} values in these crystals represent the approximate solubility limits of Nd and Pr in $BaSnO_3$, which are apparently significantly lower than that for La. This could be simply rationalized in terms of the decreasing ionic radius from La^{3+} to Pr^{3+} to Nd^{3+}, resulting in a progressively poorer match with the large Ba^{2+} ions. Further experimental and theoretical work will likely be needed, however, to determine if such a large difference in solubility can be accounted for solely based on ionic radius. Moving on to comparisons to the measured Hall electron densities, we first recall that for La doping the measured n of 3.36×10^{20} cm^{-3} agrees quite well with the La loading in the flux growth, suggesting essentially full dopant activation and negligible compensation at these doping levels. In the Nd and Pr cases, however, the n values are lower, at 1.1×10^{20} cm^{-3}. Our best estimates for N_{Nd} and N_{Pr} are 0.26 and 0.41 at. %, respectively, corresponding to 3.7×10^{19} Nd ions/cm^3 and 8.4×10^{19} Pr ions/cm^3. The estimated N_{donor} values are thus *lower* than the measured Hall electron densities. Taking into account V_O doping reconciles these two values, however. Explicitly, our measured n values from V_O doping in UD crystals under these growth conditions were consistently $\sim 3 \times 10^{19}$ cm^{-3}. Adding this value to the N_{Nd} and N_{Pr} estimates (assuming similar O deficiency in rare-earth-doped crystals) yields 0.7×10^{20} and 1.1×10^{20} cm^{-3}, respectively, in very reasonable agreement with the measured

$n = 1.1 \times 10^{20}$ cm^{-3}. Actual concentrations of rare earth dopants estimated from simple magnetometry measurements (in addition to heat capacity measurements) can thus be semi-quantitatively reconciled with measured Hall electron densities, provided additional V_O doping is also taken into account.

IV. SUMMARY

In summary, we have demonstrated the growth of Nd- and Pr-doped $BaSnO_{3-\delta}$ crystals with electronic properties, in particular mobilities that are essentially indistinguishable from La-doped versions, despite modest solubility limits. Magnetometry and heat capacity measurements of these magnetic rare-earth-doped stannate crystals have additionally been established as a simple means to directly estimate dopant concentrations. The latter have been compared to measured Hall electron densities, showing that semiquantitative reconciliation of carrier and dopant densities is possible, assuming full dopant activation and negligible compensation at these doping levels, but only provided that additional oxygen vacancy doping is also accounted for. Low temperature heat capacity measurements additionally enable extraction of effective mass values, which are in approximate agreement with recent reports. For the specific case of Pr, more complex low temperature specific heat and magnetometry behavior is observed, which we relate to crystalline electric field effects. These results thus provide significant insight into doping in $BaSnO_3$, establishing new rare earth magnetic dopants, clarifying the role of O vacancies, and determining dopant concentrations and solubility limits.

[1] A. S. Bhalla, R. Guo, and R. Roy, Mater. Res. Innov. **4**, 3 (2000).

[2] Y. Tokura and H. Y. Hwang, Nat. Mater. **7**, 694 (2008).

[3] R. Ramesh and D. G. Schlom, MRS Bull. **33**, 1006 (2008).

[4] J. Chakhalian, A. J. Millis, and J. Rondinelli, Nat. Mater. **11**, 92 (2012).

[5] J. Falson, D. Maryenko, B. Friess, D. Zhang, Y. Kozuka, A. Tsukazaki, J. H. Smet, and M. Kawasaki, Nat. Phys. **11**, 347 (2015).

[6] A. Tsukazaki, S. Akasaka, K. Nakahara, Y. Ohno, H. Ohno, D. Maryenko, A. Ohtomo, and M. Kawasaki, Nat. Mater. **9**, 889 (2010).

[7] R. D. Shannon, J. L. Gillson, and R. J. Bouchard, J. Phys. Chem. Solids **38**, 877 (1977).

[8] T. Minami, H. Sonohara, S. Takata, and H. Sato, Jpn. J. Appl. Phys. **33**, L1693 (1994).

[9] H. J. Kim, U. Kim, H. M. Kim, T. H. Kim, H. S. Mun, B.-G. Jeon, K. T. Hong, W.-J. Lee, C. Ju, K. H. Kim, and K. Char, Appl. Phys. Express **5**, 061102 (2012).

[10] H. J. Kim, U. Kim, T. H. Kim, J. Kim, H. M. Kim, B.-G. Jeon, W.-J. Lee, H. S. Mun, K. T. Hong, J. Yu, K. Char, and K. H. Kim, Phys. Rev. B **86**, 165205 (2012).

[11] X. Luo, Y. S. Oh, A. Sirenko, P. Gao, T. A. Tyson, K. Char, and S.-W. Cheong, Appl. Phys. Lett. **100**, 172112 (2012).

[12] W.-J. Lee, H. J. Kim, J. Kang, D. H. Jang, T. H. Kim, J. H. Lee, and K. H. Kim, Annu. Rev. Mater. Res. **47**, 391 (2017).

[13] A. Spinelli, M. A. Torija, C. Liu, C. Jan, and C. Leighton, Phys. Rev. B **81**, 155110 (2010).

[14] H.-R. Liu, J.-H. Yang, H. J. Xiang, X. G. Gong, and S.-H. Wei, Appl. Phys. Lett. **102**, 112109 (2013).

[15] K. Krishnaswamy, B. Himmetoglu, Y. Kang, A. Janotti, and C. G. Van de Walle, Phys. Rev. B **95**, 205202 (2017).

[16] S. Dabaghmanesh, R. Saniz, M. N. Amini, D. Lamoen, and B. Partoens, J. Phys. Condens. Matter **25**, 415503 (2013).

[17] B. G. Kim, J. Y. Jo, and S. W. Cheong, J. Solid State Chem. **197**, 134 (2013).

[18] E. Moreira, J. M. Henriques, D. L. Azevedo, E. W. S. Caetano, V. N. Freire, U. L. Fulco, and E. L. Albuquerque, J. Appl. Phys. **112**, 043703 (2012).

[19] D. O. Scanlon, Phys. Rev. B **87**, 161201 (2013).

[20] K. Krishnaswamy, L. Bjaalie, B. Himmetoglu, A. Janotti, L. Gordon, and C. G. Van de Walle, Appl. Phys. Lett. **108**, 083501 (2016).

[21] P. Zhang, F. Su, J. Dai, K. Zhang, C. Zhang, W. Zhou, Q. Liu, and L. Pi, Europhys. Lett. **106**, 67005 (2014).

[22] C. Shan, T. Huang, J. Zhang, M. Han, Y. Li, Z. Hu, and J. Chu, J. Phys. Chem. C **118**, 6994 (2014).

[23] D. Seo, K. Yu, Y. J. Chang, E. Sohn, and K. H. Kim, Appl. Phys. Lett. **104**, 022102 (2014).

[24] U. Kim, C. Park, T. Ha, R. Kim, H. S. Mun, H. M. Kim, H. J. Kim, T. H. Kim, N. Kim, J. Yu, K. H. Kim, J. H. Kim, and K. Char, APL Mater. **2**, 056107 (2014).

[25] C. A. Niedermeier, S. Rhode, S. Fearn, K. Ide, M. A. Moram, H. Hiramatsu, H. Hosono, and T. Kamiya, Appl. Phys. Lett. **108**, 172101 (2016).

[26] C. A. Niedermeier, S. Rhode, K. Ide, H. Hiramatsu, H. Hosono, T. Kamiya, and M. A. Moram, Phys. Rev. B **95**, 161202 (2017).

[27] S. James Allen, S. Raghavan, T. Schumann, K. M. Law, and S. Stemmer, Appl. Phys. Lett. **108**, 252107 (2016).

[28] H. J. Kim, J. Kim, T. H. Kim, W.-J. Lee, B.-G. Jeon, J.-Y. Park, W. S. Choi, D. W. Jeong, S. H. Lee, J. Yu, T. W. Noh, and K. H. Kim, Phys. Rev. B **88**, 125204 (2013).

[29] Z. Lebens-Higgins, D. O. Scanlon, H. Paik, S. Sallis, Y. Nie, M. Uchida, N. F. Quackenbush, M. J. Wahila, G. E. Sterbinsky, D. A. Arena, J. C. Woicik, D. G. Schlom, and L. F. J. Piper, Phys. Rev. Lett. **116**, 027602 (2016).

[30] C. Park, U. Kim, C. J. Ju, J. S. Park, Y. M. Kim, and K. Char, Appl. Phys. Lett. **105**, 203503 (2014).

[31] J. Shiogai, K. Nishihara, K. Sato, and A. Tsukazaki, AIP Adv. **6**, 065305 (2016).

[32] J. Shin, Y. M. Kim, Y. Kim, C. Park, and K. Char, Appl. Phys. Lett. **109**, 262102 (2016).

[33] W.-J. Lee, H. J. Kim, E. Sohn, T. H. Kim, J.-Y. Park, W. Park, H. Jeong, T. Lee, J. H. Kim, K.-Y. Choi, and K. H. Kim, Appl. Phys. Lett. **108**, 082105 (2016).

[34] K. Ganguly, P. Ambwani, P. Xu, J. S. Jeong, K. A. Mkhoyan, C. Leighton, and B. Jalan, APL Mater. **3**, 062509 (2015).

[35] K. Ganguly, A. Prakash, B. Jalan, and C. Leighton, APL Mater. **5**, 056102 (2017).

[36] H. Paik, Z. Chen, E. Lochocki, A. H. Seidner, A. Verma, N. Tanen, J. Park, M. Uchida, S. Shang, B.-C. Zhou, M. Brutzam, R. Uecker, Z.-K. Liu, D. Jena, K. M. Shen, D. A. Muller, and D. G. Schlom, APL Mater. **5**, 116107 (2017).

[37] S. Raghavan, T. Schumann, H. Kim, J. Y. Zhang, T. A. Cain, and S. Stemmer, APL Mater. **4**, 016106 (2016).

[38] A. Prakash, P. Xu, X. Wu, G. Haugstad, X. Wang, and B. Jalan, J. Mater. Chem. C **5**, 5730 (2017).

[39] A. Prakash, P. Xu, A. Faghaninia, S. Shukla, J. W. Ager, C. S. Lo, and B. Jalan, Nat. Commun. **8**, 15167 (2017).

[40] T. N. Stanislavchuk, A. A. Sirenko, A. P. Litvinchuk, X. Luo, and S.-W. Cheong, J. Appl. Phys. **112**, 044108 (2012).

[41] L. Weston, L. Bjaalie, K. Krishnaswamy, and C. G. Van de Walle, Phys. Rev. B **97**, 054112 (2018).

[42] Z. Galazka, R. Uecker, K. Irmscher, D. Klimm, R. Bertram, A. Kwasniewski, M. Naumann, R. Schewski, M. Pietsch, U. Juda, A. Fiedler, M. Albrecht, S. Ganschow, T. Markurt, C. Guguschev, and M. Bickermann, J. Phys. Condens. Matter **29**, 075701 (2017).

[43] H. J. Kim, T. H. Kim, W.-J. Lee, Y. Chai, J. W. Kim, Y. J. Jwa, S. Chung, S. J. Kim, E. Sohn, S. M. Lee, K.-Y. Choi, and K. H. Kim, Thermochim. Acta **585**, 16 (2014).

[44] U. S. Alaan, P. Shafer, A. T. N'Diaye, E. Arenholz, and Y. Suzuki, Appl. Phys. Lett. **108**, 042106 (2016).

[45] J. C. Lashley, M. F. Hundley, A. Migliori, J. L. Sarrao, P. G. Pagliuso, T. W. Darling, M. Jaime, J. C. Cooley, W. L. Hults, L. Morales, D. J. Thoma, J. L. Smith, J. Boerio-Goates, B. F. Woodfield, G. R. Stewart, R. A. Fisher, and N. E. Phillips, Cryogenics (Guildf) **43**, 369 (2003).

[46] J. Jensen and A. R. Mackintosh, *Rare Earth Magnetism: Structures and Excitations* (Clarendon, Oxford, 1991).

[47] A. Furrer, A. Podlesnyak, M. Frontzek, I. Sashin, J. P. Embs, E. Mitberg, and E. Pomjakushina, Phys. Rev. B **90**, 064426 (2014).

[48] W. G. Penney and R. Schlapp, Phys. Rev. **41**, 194 (1932).

[49] H. M. Rosenberg, *Low Temperature Solid State Physics* (Oxford University Press, New York, 1963).

[50] E. S. R. Gopal, *Specific Heats at Low Temperatures* (Plenum, New York, 1966).

[51] T. Maekawa, K. Kurosaki, and S. Yamanaka, J. Alloys Compd. **416**, 214 (2006).

[52] A. Bouhemadou and K. Haddadi, Solid State Sci. **12**, 630 (2010).

[53] D. Phelan, F. Han, A. Lopez-Bezanilla, M. J. Krogstad, Y. Gim, Y. Rong, J. Zhang, D. Parshall, H. Zheng, S. L. Cooper, M. Feygenson, W. Yang, and Y.-S. Chen, J. Solid State Chem. **262**, 142 (2018).

[54] Y. Hinatsu, J. Solid State Chem. **122**, 384 (1996).

[55] O. Guillot-Noël, P. Goldner, F. Beaudoux, Y. Le Du, J. Lejay, A. Amari, A. Walther, L. Rippe, and S. Kröll, Phys. Rev. B **79**, 155119 (2009).